Contents lists available at Egyptian Knowledge Bank

Labyrinth: Fayoum Journal of Science and Interdisciplinary Studies

Journal homepage: https://lfjsis.journals.ekb.eg/

A comparative study between the physical properties of polyacrylonitrile loaded with 10 wt.% of strontium hexaferrite and those with the same content of nickel cobaltite nanoparticles

Walaa M. Shoubak [a], A. Hassan [a], S. Mahrous [a], A. Hassen [a,*]

[a] Physics Department, Faculty of Science, Fayoum University, El Fayoum 63514, Egypt.

ARTICLE INFO

Keywords:

Strontium hexaferrite (SFO); Nickel cobaltite (NCO); polyacrylonitrile (PAN); nanocomposites; characterizationand dielectric; properties.

ABSTRACT

This study reports a comparative analysis between two different nanocomposite films that were synthesized by the casting method. Polyacrylonitrile (PAN) loaded with 10 wt. % strontium hexaferrite ($SrFe_{12}O_{19}$, SFO) nanoparticles (NPs). Similarly, the same content of nickel cobaltite ($NiCo_2O_4$, NCO) NPs-doped PAN was prepared. X-ray diffraction (XRD) patterns revealed a successful formation of both two nanocomposite films. According to the result of the thermal analysis, both NCO and SFO NPs enhanced the thermal stability of the PAN matrix. Field emission-scanning electron microscopy (FE-SEM) and Fourier transform infrared (FTIR) are used to characterize the studied noncomposite films. The dielectric properties of PAN were enhanced with doping and the 10 wt.% NCO NPs/PAN showed higher dielectric permittivity, ac conductivity, and lower dielectric losses compared to those of the same SFO nanocomposite film. It was found that the dielectric parameters were significantly dependent on the type of nanofiller. NCO/PAN nanocomposite film could be a potential candidate for storage energy components.

1. Introduction

Recently, the field of polymer nanocomposites (PNC) has attracted considerable attention. Compared to pure polymers, the material properties of the nanocomposites are significantly improved, and they have a wide range of potential applications like optoelectronic devices, reflective materials, magneto-optic, data storages, and photovoltaic cells [1-3]. Much work has been done to improve the properties of polymer nanocomposites by reinforcing polymers with metals, carbon nanotubes, semiconductors, and magnetic nanoparticles [4-7]. These factors have led researchers to choose Polyacrylonitrile (PAN) as the host matrix for creating large, advanced PNC materials with the right quantity of inorganic and/or organic nanofillers dispersed for their technological applications. PAN is the subject of intensive research due to its high strength [8], thermal stability [9], abrasion resistance [10], and suitability as a precursor for the production of carbon. In addition, PAN is completely non-toxic, suitable for biological uses, and useful in biomedical applications [11-12].

Researchers have recently shown a lot of interest in NPCs based on PAN owing to their unique physicochemical properties, such as enhanced mechanical properties [13], magnetic properties [14], and higher conductivity [15], which allow a variety of applications for these materials. Strontium hexaferrite, ($SrFe_{12}O_{19}$ or SFO) has drawn a lot of interest due to its saturation magnetization, high coercivity, Curie temperature, and magnetocrystalline anisotropy [16-17]. Also, SFO has been used as, permanent magnets, in communications, and magneto-optical technologies [18]. In our earlier research, we synthesized SFO nanoparticles (NPs)/PAN nanocomposites with different content of SFO NPs [19]. The physical properties such as the optical, dielectric, and magnetic characteristics of these nanocomposites were reported.

On the other hand, spinel nickel cobaltite ($NiCo_2O_4$ or NCO) has been used as a multifunctional transition nanometal oxide. More importantly, NCO has many significant physical and chemical properties, good electron conductivity [20], and high pseudo-capacitive performance [21]. These unique properties make NCO superior in electrochemical storage devices. According to the literature, most works concerned with polymer nanocomposites filled with NCO NPs focus on their electrochemical properties [22-26]. However, the dielectric, and optical properties of nanocomposites are rarely discussed. Therefore, the incorporation of NCO NPs into the polyacrylonitrile is important to have good nanocomposites for applications. Therefore, the impact of different content of NCO NPs on the physical properties of PAN was also reported [27].

This work aims to compare the physical properties of SFO and NCO NPs-doped PAN at 10 wt. %. level of doping. The as-prepared nanocomposite films were characterized by using different techniques. The physical properties of the two nanocomposite films such as dielectric, and optical properties were discussed. This comparison is done to show the mechanisms and applications of each nanocomposite film.

2. Materials and Methods

The supplier of polyacrylonitrile (PAN; Mw~150,000g mol-1) was polymer laboratories, located in Essex, UK. The used chemical oxides of the as-prepared nickel cobaltite ($NiCo_2O_4$ or NCO), strontium hexaferrite ($SrFe_{12}O_{19}$ or SFO), and dimethylformamide (DMF, 99.9%), were purchased from

Aldrich, Germany. All of the chemicals were used exactly as received, without any additional purification, and are of analytical quality. The nanocomposite films were prepared as follows:

The 10 wt. % of both SFO and NCO NPs were added to PAN according to:

$$x\ (\text{wt.}\%) = \frac{w_f}{w_f + w_p} \qquad (1)$$

where w_f and w_p represent the corresponding weights of both nanofilers and PAN, respectively. The PAN powder was dissolved in 25 mL of dimethyl formamide (DMF) solution and magnetically stirred for 12 h at room temperature (RT) until a clear solution was obtained. The desired amount of nanofilers was dispersed in 15 mL of DMF solution separately via ultra-sonication for 3 h at RT. Then the mixture of both PAN and each nanofiller was sonicated for 3 hrs in DMF solvent. For the film formation, the product was spread uniformly onto clean glass Petri dishes by casting and then dried inside an oven set to 70 °C for 8 h. More information about sample preparation is in our most recent publications [19, 27].

Using a Fourier transform infrared spectrometer (FTIR) in the $4x10^2$–$40x10^2$ cm^{-1} wavenumber range (JASCO, FT/IR-6200), Fourier transform infrared (FT-IR) charts of the samples were obtained. Focused on pure PAN and nanocomposite films, field emission scanning electron microscopy (FE – SEM Carl Zeiss Sigma 500VP, Holland) was used to examine the surface properties. Cu-K_α radiation was used in the X'Pert PRO diffractometer by PAN analytical to obtain the XRD patterns. With the use of Perkin Elmer STA 6000 N_2 atom DSC and TGA (Q50, TA instruments), the thermal properties of the samples were examined. A Hioki model 3532 High Tester LCR (Ueda, Nagano, Japan) was used to measure dielectric properties. The dielectric permittivity, ε', and dielectric loss factor, ε", were calculated ($\varepsilon' = d\,C/\varepsilon_0 A$, $\varepsilon'' = \varepsilon' \tan\delta$, where d is the sample thickness, C is the capacitance of the sample-filled capacitor, ε_0 is the vacuum permittivity, and A is the electrode area) at different ranges of frequency and temperature. UV-vis spectrophotometer (JASCO 630) in the wavelength range (λ) of $2x10^2$ – $8x10^2$ nm was used to determine the optical characteristics at room temperature (RT).

3. Results and discussions

3.1. Material characterization

For comparison, Fig. 1 displays the FTIR spectra of pure PAN, PAN doped with 10% weight percentage SFO NPs, and PAN doped with the same amount of NCO NPs. Four characteristic peaks of PAN appeared at 1480, 2930, 2250, and 1680 cm^{-1} could be related to the bending, stretching methylene (CH_2) groups, the strong stretching vibration of nitrile groups (-CN-), and the carbonyl group (CO stretch), respectively [27,28]. Furthermore, the peaks at 1200 and 1370 cm^{-1} were attributed to the CN stretch and the aliphatic C–H bend, respectively [28].

Moreover, the CN stretch and the aliphatic C-H bend, respectively, were identified as the sources of the peaks at 1200 and 1370 cm^{-1} [28]. The FTIR spectra of PAN loaded with 10 weight percent NCO is observed to be nearly identical to that of PAN. Additionally, there was a minor shift in the PAN's spectrum when the 10% SFO nanocomposite film was added. The reason for this shift is that, in tetrahedral and octahedral binding, the bond length between Fe^{3+}- O^{2-} ions varies [29]. This could suggest that SFO NPs

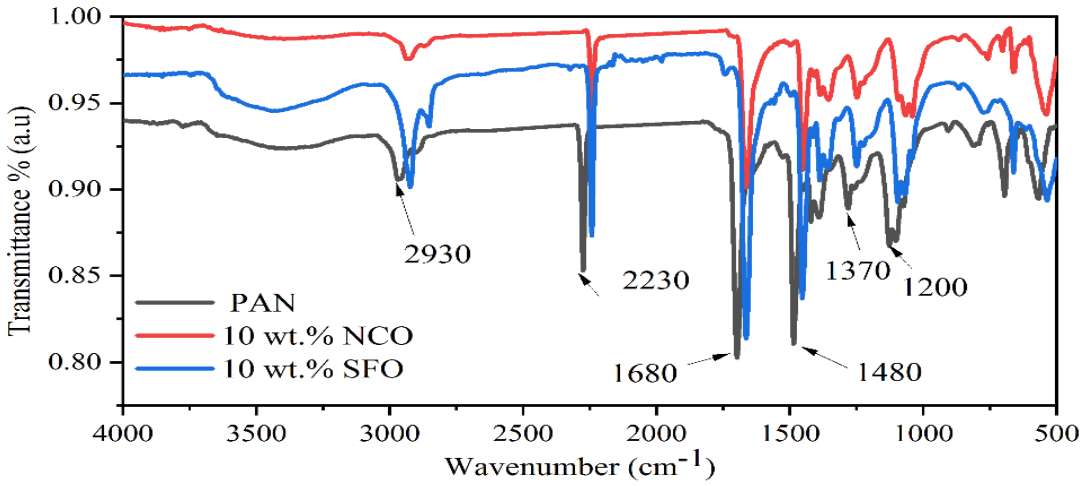

Fig 1: FTIR spectra of pure PAN and PAN doped with 10wt.% NCO as well as with SFO NPs.

The FE-SEM images of pure SFO and NCO NPs with the two nanocomposite films are depicted in Fig. 2 (a-d). Both SFO and NCO NPs showed a hexagonal shape with different particle arrangements (see Fig. 2 (a, c)). A distribution of SFO NPs in the PAN matrix was observed (Fig. 2(b)) compared to NCO NPs (Fig. 2(d)). As seen in Fig. 2 (d), the distribution of NCO NPs in the PAN is not homogeneous because of an agglomeration of this nanofiller compared to that of SFO NPs. Such relative changes in the morphology of the studied two nanocomposite films can be attributed to the different ways of interacting nanofillers with the PAN structures, and also their chemical nature.

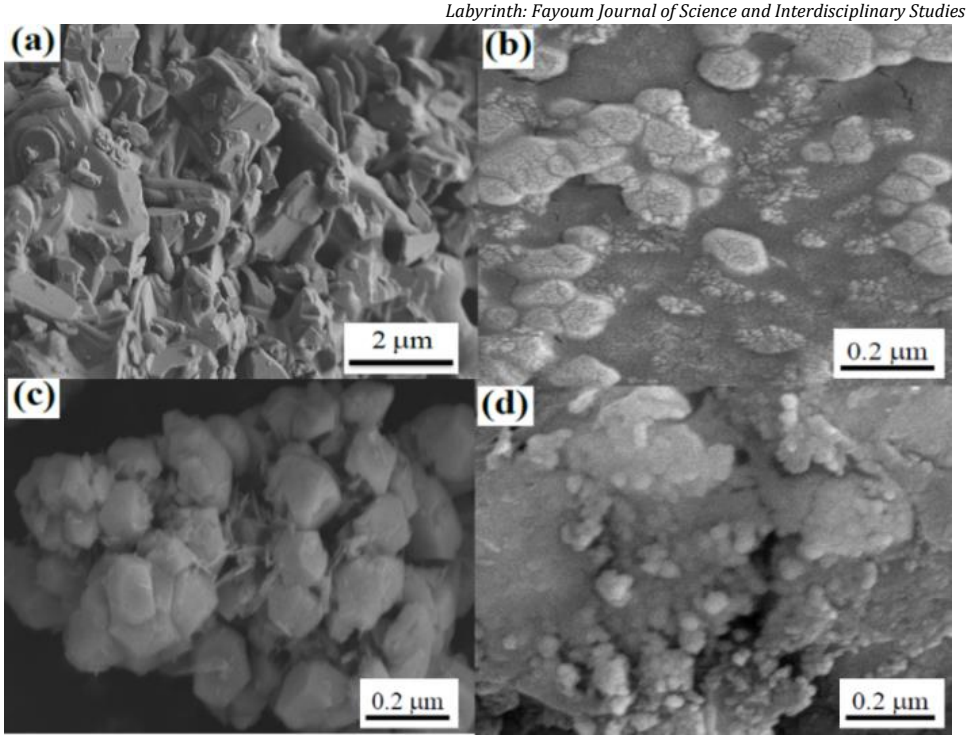

Fig 2. Field emission-scanning electron microscopy (FE-SEM) images of the as-prepared samples (a) SFO NPs, (b) PAN loaded with 10 wt.% SFO nanocomposite film, (c) NCO NPs, and (d) PAN doped with 10 wt.% NCO nanocomposite film.

To compare the XRD patterns of both nanocomposite films, Figure 3 includes the patterns of pure NPs as well as pure PAN. The characteristic peaks of PAN, SFO, and NCO NPs were previously investigated [19, 27]. On the other hand, the XRD patterns of PAN doped with 10 wt.% SFO and NCO NPs exhibited characteristic diffraction peaks corresponding to the crystalline structures of the respective NPs. This confirms their presence in the PAN matrix. It is also noticed that the positions of these peaks didn't change when dispersed in the host PAN matrix indicating that the nanofillers preserved their original structures in the PAN matrix. The mean crystallite size of both SFO and NCO nanoparticles was calculated based on the Debye-Scherrer formula [30]. The average crystallite size of SFO and NCO NPs was found to be 48 nm [19] and 16 nm [27], respectively. It is also observed from the XRD pattern of PAN doped with 10 wt.% NCO nanocomposite film that the polymer main characteristic peak (at $2\theta = 17^{o}$) has a lower intensity than that of 10 wt.% SFO-doped PAN which reflects a decrease in the degree of crystallinity. Therefore, the degree of crystallinity (Xc) of the samples was determined using Hinrichen's approach [31]:

$$X_c = \frac{I_C}{I_c + I_a} \quad 100\% \qquad (2)$$

Where Ic refers to the integral area of the crystalline portion and Ia refers to the integral area of the amorphous zone in the XRD patterns. The calculated values of the Xc are listed in Table 1. The comparative study demonstrated that the PAN degree of crystallinity increased by adding 10 wt.% SFO while it decreased by introducing the same content of NCO NPs. There is an ability of SFO NPs to enforce the alignment of the PAN polymer chain whereas the NCO NPs disrupted the regular macromolecules of PAN. The specific surface chemistry, size, or shape of NCO NPs may lead to unfavorable interactions with PAN, disrupting the polymer's regular structure. The different effects between SFO and NCO NPs emphasize that the type and characteristics of nanoparticles play a crucial role in their interaction with polymers.

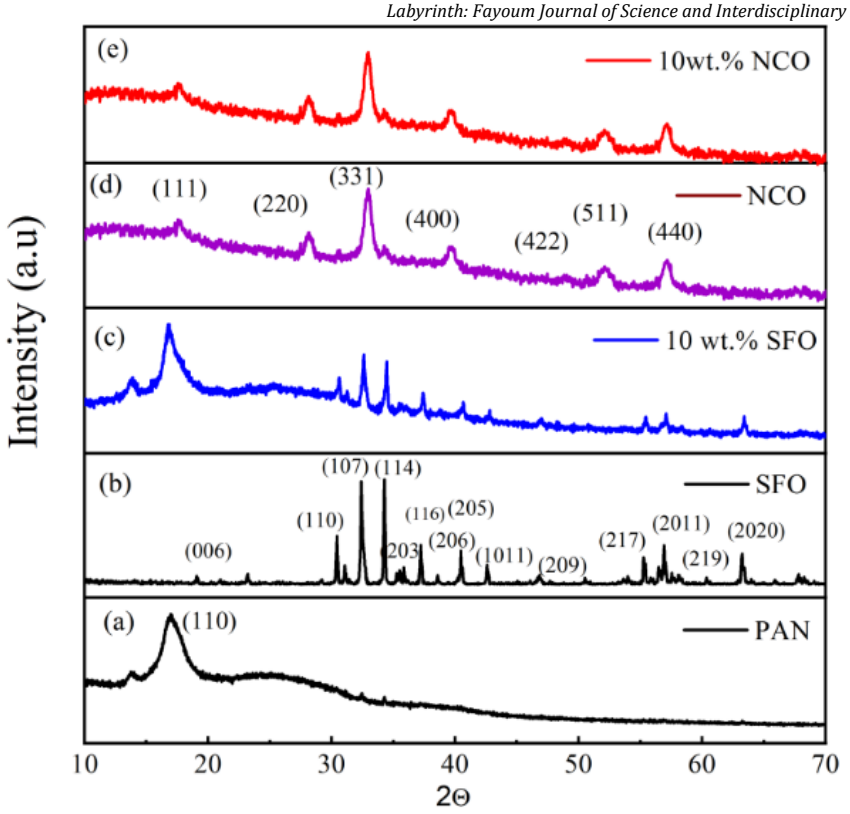

Fig 3. The XRD spectra of (a) pure PAN, (b) SFO NPs, (c) 10 wt.% SFO NPs,-doped PAN (d) NCO NPs, and (e) PAN doped with 10 wt.% NCO NPs.

The heating scan thermogram for the studied nanocomposite films is shown in Figure 4. The DSC profiles present a crystallization temperature peak (T_C) without a melting peak within the studied range of temperatures. PAN exhibits an exothermic peak at 297 °C [19, 27]. One noted that the T_C decreases with the incorporation of both nanoparticles into the polymer matrix. More decrease is observed in the case of NCO NPs–doped PAN compared to SFO ones. The decrease in TC for the PAN doped with 10 wt.% NCO NPs is perhaps due to the nonhomogeneous morphology of these NPs as seen from the FE-SEM image. In addition, a decrement of the crystallization enthalpy (ΔHc) (see Table 1) is observed by adding the same content of both SFO and NCO NPs to the PAN matrix. In addition, ΔHc of the SFO/PAN noncomposite film is higher than that of the NCO/PAN probably due to the enforcement of SFO NPs to align the polymer matrix and therefore increase the degree of crystallinity.

Table 1: Thermal parameters of pure PAN, and PAN doped with 10wt.% SFO as well as NCO NPs.

Sample	T_C°C	ΔHC (Jg^{-1})	Residual Weight at 800 C (%)	X_C (%)
Pure PAN	297	449	54	23.30
10 wt.% SFO	284	335	64	26.40
10 wt.% NCO	270	283	67	21.09

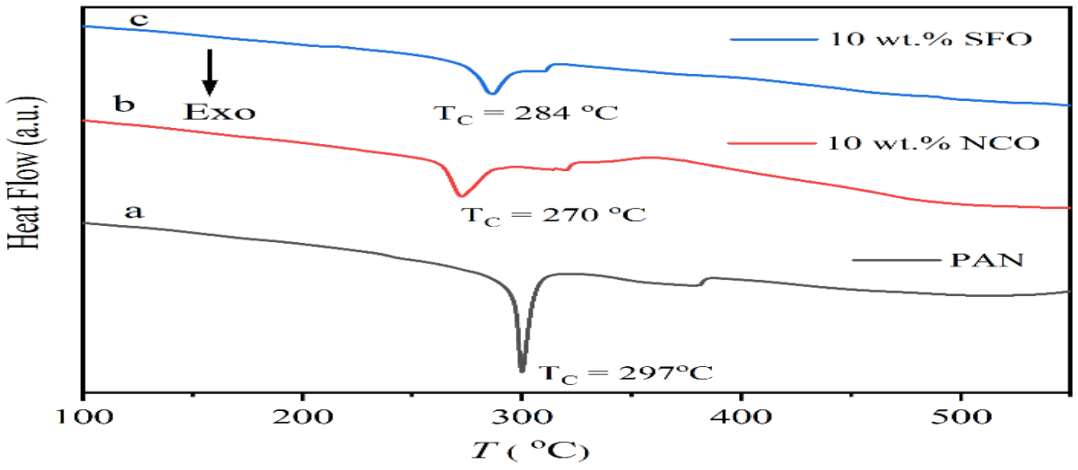

Fig 4: DSC analysis of pure PAN, and PAN loaded with 10 wt.% SFO as well as NCO NPs.

Figure 5 shows TGA curves of pure PAN and the as-prepared nanocomposite films. Four stages of degradation can be identified; the initial weight loss begins around 50 oC ascribed to the loss of water molecules and low molecular weight oligomers [32]. The second stage of degradation occurred at 290 – 350 oC is due to nitrile oligomerization. In the third and fourth stages, between 350 and 600 oC, the weight loss observed for all tested samples was due to pyrolytic degradation of PAN leaving residual masses near 600 oC, of 54 %, 64%, and 67%, for pure PAN, and PAN doped with 10 wt.% SFO and NCO, respectively. Comparative curves showed that the decomposition of nanocomposite films happens slowly as compared to that of pure PAN. This implies that the incorporation of both SFO and NCO NPs into PAN polymer matrix displayed a stabilization effect against decomposition. Additionally, the nanocomposite film containing 10 wt.% NCO NPs is more thermally stable than PAN loaded with 10 wt.% SFO NPs. This is probably due to the difference in the surface morphology of the two nanocomposite films.

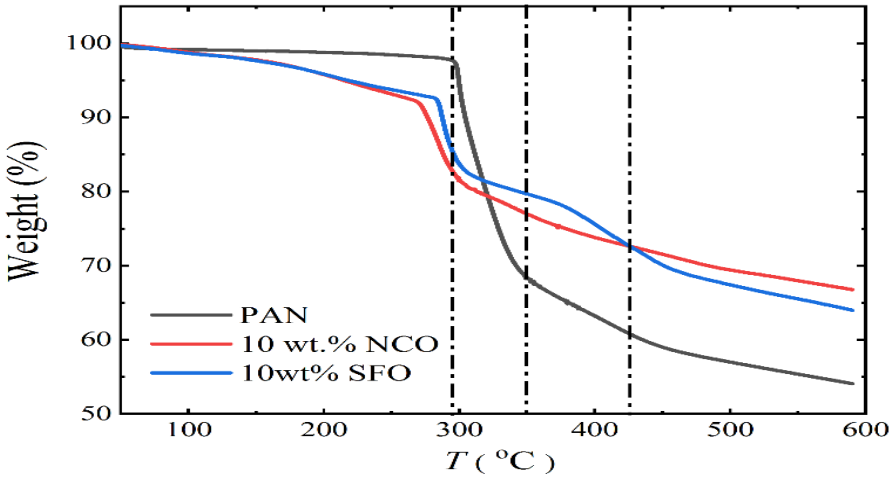

Fig 5: TGA curves of pure PAN, and PAN loaded with 10wt.% SFO as well as NCO NPs.

٣،٢. Dielectric characteristics

The characteristics of dielectric for both 10 wt.% SFO and NCONPs–doped PAN were studied. The frequency dependence of ε' for all samples is shown in Fig. 6(a-d). It is observed that the value of ε' decreases with increasing frequency. At lower frequencies, the dipoles could align themselves along the field and therefore contribute completely to the polarization of the dielectric materials. At higher frequencies, the variation in the field is too fast and the dipoles are no longer able to align the field, so their contribution to the polarization becomes negligible. As a result, the dielectric permittivity decreases as frequency increases. Interestingly, the addition of 10 wt.% SFO and NCO nanoparticles to the PAN matrix enhanced the ε′ values. Besides, the dielectric permittivity values of PAN doped with 10 wt.% NCO NPs are higher than that of nanocomposite film containing 10 wt.% SFO NPs. This may be due to NCO NPs having higher dielectric permittivity due to their spinal structure where Ni, Co, and O form a cubic close-packed structure, and both Ni and Co ions can undergo charge redistribution leading to an increase of polarization.

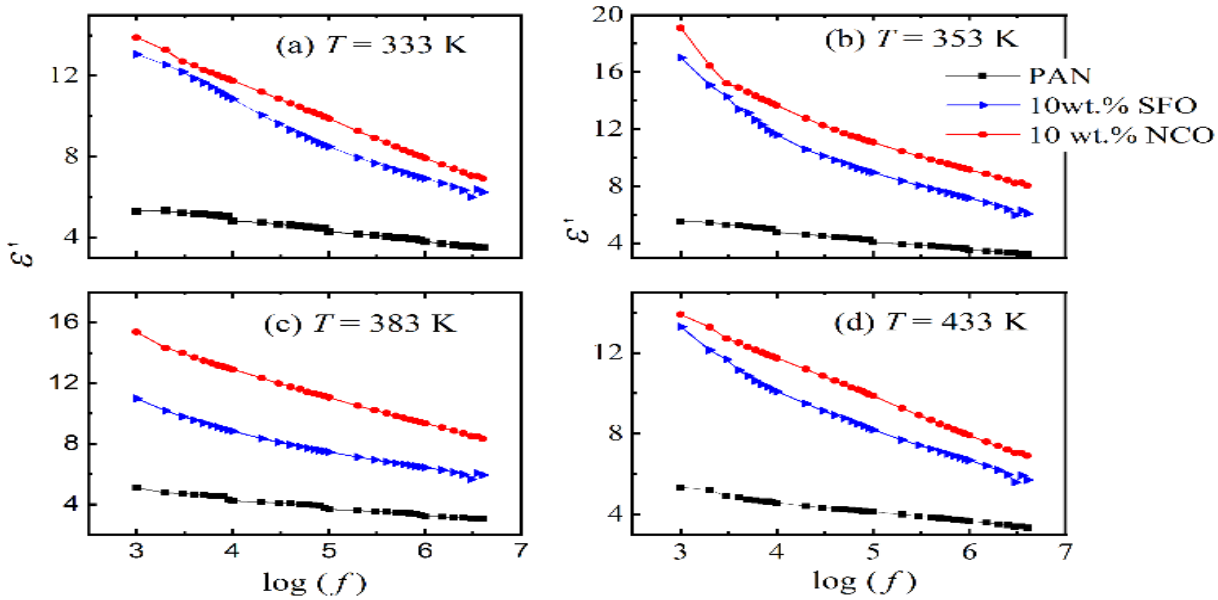

Fig 6: Comparison of real dielectric permittivity as a function of frequency of pure PAN and PAN doped with 10 wt.% SFO and NCO NPs at different fixed temperatures

The variation of ε′ with temperature for pure PAN and PAN doped with 10 wt.% SFO and NCO NPs is shown in Figure 7(a-c). At low temperatures, the segmental motion of the chain is completely frozen which reduces the dielectric permittivity. By increasing temperature, the dipoles acquire sufficient energy to align themselves easily in the direction of the applied electric field which enhances ε'. At sufficiently higher temperatures, the dielectric permittivity is lowered again owing to strong thermal motion that disturbs the orientation of the dipoles.

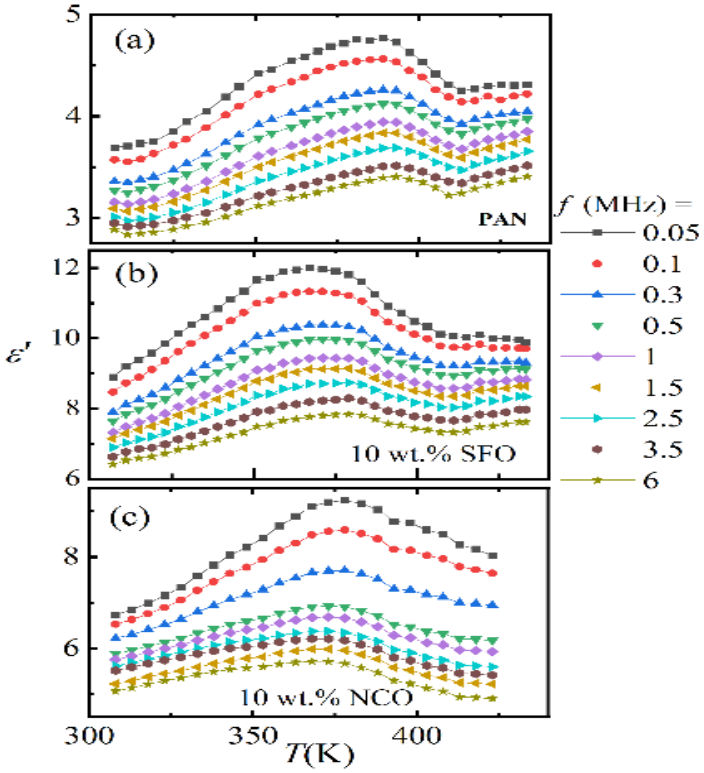

Fig 7 (a-c): The dielectric permittivity as a function of temperature at different selected frequencies for (a) pure PAN, (b) PAN doped with 10 wt.% SFO, and (c) NCO NPs nanocomposite films.

Figure 8 displayed the frequency dependence of the dielectric loss, ε'', for pure PAN and PAN doped with 10 wt.% SFO and NCO NPs at some selected temperatures. As observed " attain higher values at lower frequencies indicating the domination of electrode polarizations [33]. A comparative study of the dielectric loss of the as-prepared nanocomposite films showed that the PAN doped with 10 wt.% NCO NPs exhibited better dielectric loss than that of PAN doped with 10 wt.% SFO NPs. The dielectric loss of a nanocomposite is also affected by crystallinity, density, uniform distribution of nanofiller in the polymer matrix, and interaction between the nanofiller and polymer. The high dielectric loss in the PAN loaded with 10 wt.% SFO NPs could originate from the magnetic character, leading to poor interfacial adhesion between the SFO NPs. In addition, more energy is required for electron exchange between Fe^{3+} and Fe^{2+} due to the high resistance of grain boundaries which causes high energy loss [34]. The decrease of the dielectric loss of the PAN loaded with 10 wt.% NCO nanocomposite film may be due to the ionic charge balance of Ni^{2+}, Ni^{3+}, Co^{2+}, and Co^{3+}.

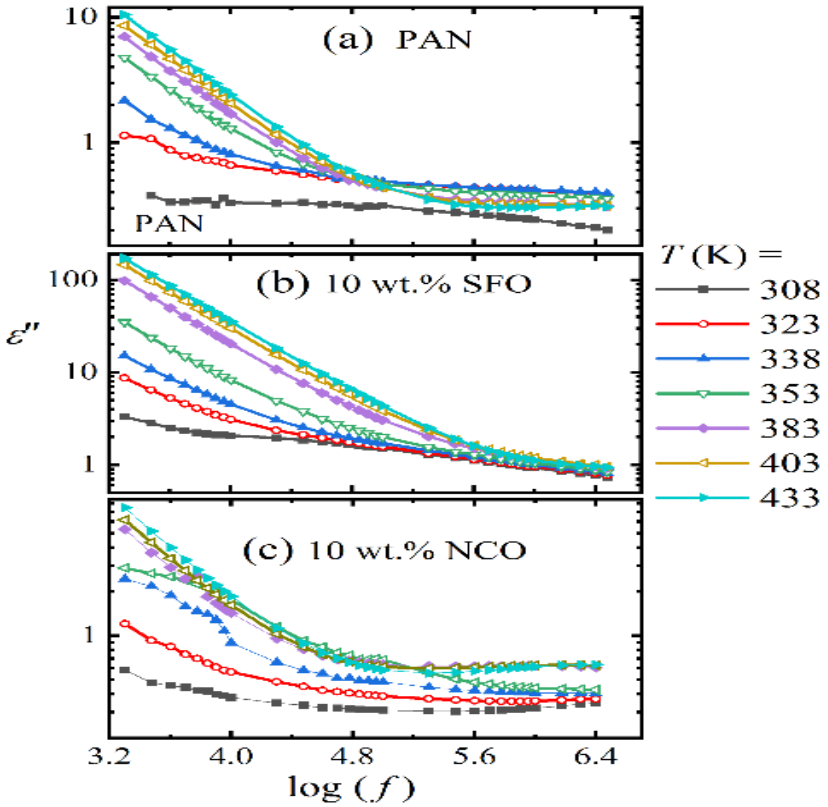

Fig 8 (a-c): Comparison of dielectric loss, as a function of frequency for (a) pure PAN, (b) PAN doped with 10 wt.% SFO NPs, and (c) PAN load with the same content of NCO NPs.

Figure 9 represents the variation of ε" with temperature for the as-prepared PAN and nanocomposite films at some selected frequencies. It is observed that the ε''(T) for both pure PAN and nanocomposite samples shows a relaxation peak suggesting a dielectric relaxation process called -relaxation. This peak appears around Tg of the polymer due to the micro-Brownian segmental motion of polymeric chains. At higher frequencies, the peak widens and changes to a higher temperature. This broadening suggests dispersion in relaxation time due to the rise in dipole density. Moreover, the peak position of α-process, at 0.05 MHz, for pure PAN and 10 wt.% NCO NPs-doped PAN is located around 375 K whereas it observed around 363 K in the case of PAN doped with 10 wt.% SFO NPs. The addition of 10 wt.% SFO NPs to PAN decreased Tg of PAN suggesting that this nanofiller could be a plasticizer for PAN.

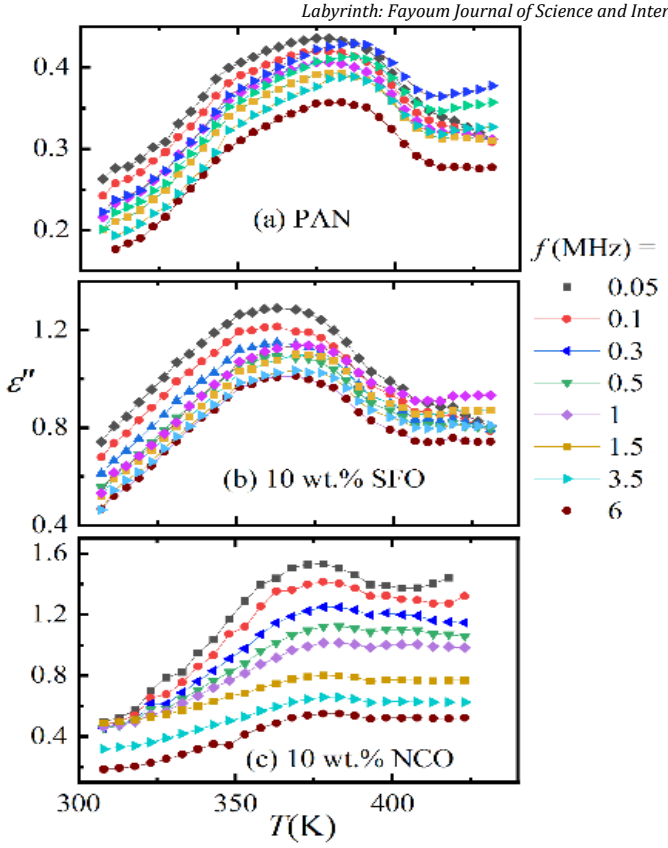

Fig 9 (a-c): Comparison of dielectric loss, ε'', as a function of temperature for (a) pure PAN and (b) PAN loaded with 10 wt.% SFO and PAN doped with the same content of NCO NPs

The main advantage of studying the dielectric modulus is to prevent electrode polarizations that can be expressed as [35]:

$$M' = \frac{\epsilon'}{\epsilon'^2 + \epsilon''^2} \quad (3)$$

$$M'' = \frac{\epsilon''}{\epsilon'^2 + \epsilon''^2} \quad (4)$$

where the real and imaginary components of the electric modulus are denoted by M' and M'', respectively. Figure 10 (a-d) displays comparative plots of M' of the studied samples as a function of temperature at some constant frequencies. The values of M' decreased with increasing temperatures tending to reach a constant value at higher temperatures. This is because the dielectric constant is thermally activated [36]. Interesting is to note that PAN doped with 10 wt.% NCO NPs nanocomposite film shows lower values of M' compared to that of PAN and PAN loaded with 10 wt.% SFO NPs consistent with the values of the dielectric permittivity.

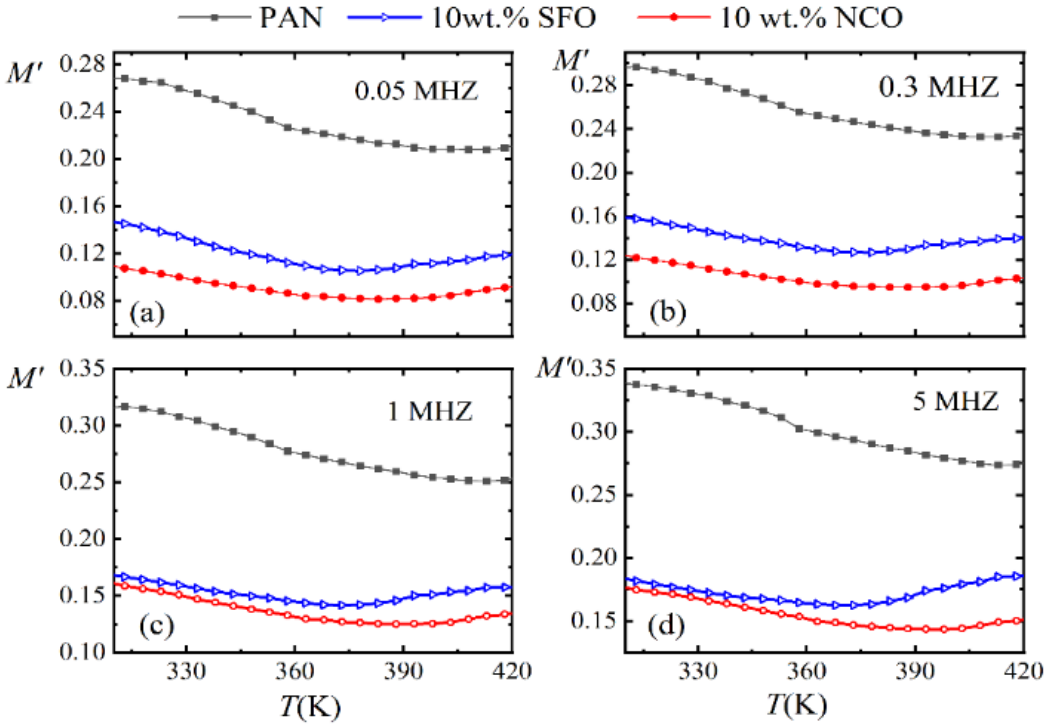

Fig 10 (a-d): A plot of real dielectric modulus as a function of temperature for pure PAN and PAN doped with 10 wt.% SFO and NCO NPs at different temperatures.

A relaxation peak was observed in the plot of M'' versus frequency for all samples (Fig. 11(a-d)). This relaxation peak is known as the conductivity-relaxation peak of the mobile ions (α_c– relaxation) [37]. It is observed that the peak intensity decreases with the addition of either 10 wt. % SFO or NCO NPs due to increasing the free charge carrier concentration within the polymer matrix. At the same time the peak shifts to a higher frequency side in the case of the 10 wt.% SFO NPs-doped PAN nanocomposite sample as compared to both pure PAN and PAN doped with 10wt.% NCO NPs which confirm that this relaxation process is significantly affected by the type of nanofiller. This shift towards higher frequencies corresponds to a reduction of relaxation time (τ) due to the inversely proportional relationship between τ maximum frequency, fmax, ($\tau = \frac{1}{2\pi f_{max}}$) [38]. Such behavior can be attributed to the interaction between the SFO NPs and PAN matrix confirmed by FTIR.

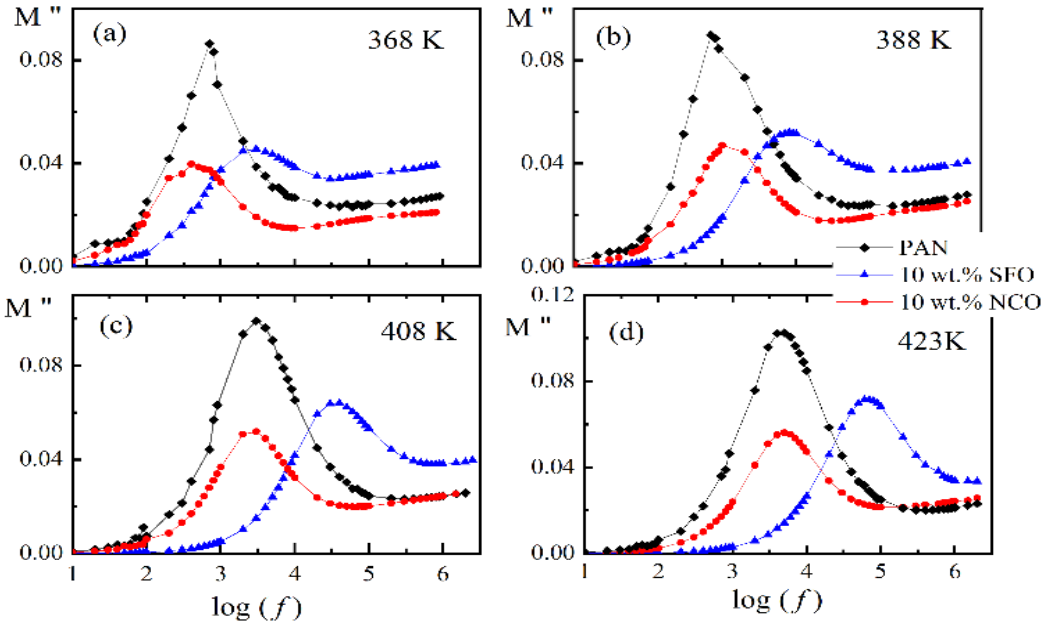

Fig 11 (a-d): A plot of M'' as a function of frequency of pure PAN and PAN doped with 10 wt.% SFO and NCO NPs at different temperatures.

The temperature dependence of the fmax follows the Arrhenius relation [39]:

$$f_{max} = f_o \exp\left(-\frac{E_a}{K_B T}\right) \quad (5)$$

where *E*a is the activation energy, for a certain relaxation process, *f*o is a characteristic constant parameter, and KB is the Boltzmann constant. Figure 12 depicts the change of ln (f_{max}) versus 1000/T for pure PAN and both nanocomposite films. The recorded principles of *E*a are given in Table 2. It is worth noting that the activation energy of the PAN decreased when it loaded with 10 wt.% SFO NPs while it increased as it was loaded with the same ratio of NCO NPs. This result could be attributed to the variation in the delocalized charge carriers in different samples.

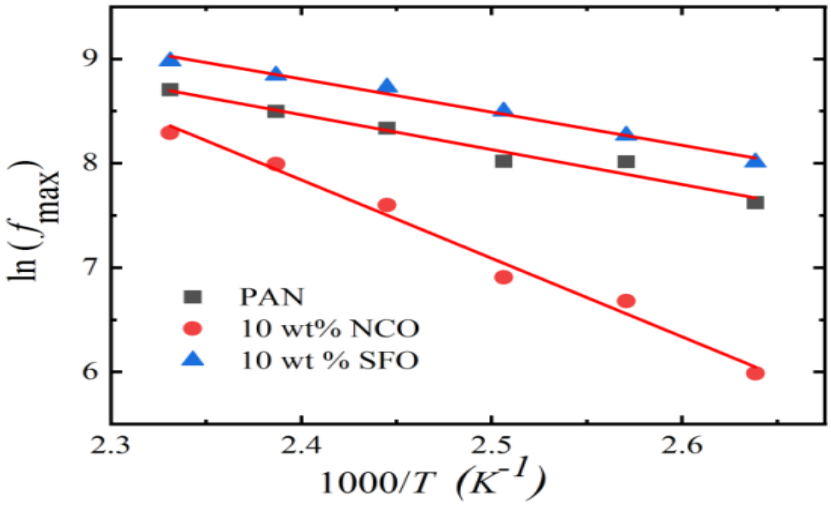

Fig 12: The variance of ln (fmax) versus 1000/T for the pure PAN and PAN loaded with 10 wt.% SFO and NCO NPs. The solid lines are the fitting according to Eq. 5.

The ac conductivity values of the samples are estimated using Eq ($\sigma_{ac} = \omega\varepsilon_o\varepsilon' tan\delta = 2\pi f \varepsilon_o \varepsilon''$) and the measured values of ac conductivity are summarized in Table 2. Both nanocomposite films exhibited higher conductivity than that of PAN. A higher σac is observed for 10 wt.% NCO-doped PAN nanocomposite sample compared to that of 10 wt.% SFO doped one. This improved conductivity may result from a combination of Ni^{2+} and Co^{3+} ions in the spinel structure of NCO that occupy the cation sub-lattice simultaneously [40]. The conductivity ac depends on frequency according to the universal dynamic response given by [41] :

$$\sigma_{ac}(\omega) = \sigma_t - \sigma_{dc} = B\,\omega^S \quad (6)$$

where σ_{dc} represents the DC conductivity, σt gives the total conductivity, B is a preexponential factor, and *S* is the universal frequency exponent. A plot of log (σ_{ac}) versus log (*f*) for pure PAN and PAN doped with 10 wt.% SFO as well as 10 wt.% NCO NPs is illustrated in Fig. 13.

The frequency exponent, S, at different temperatures, was calculated from the slopes of the fitting of the ac conductivity to identify the type of conduction mechanism. The values of S for both pure PAN and PAN doped with 10 wt.% SFO and NCO NPs are given in Table 2. As seen, the values of S are less than 1 for all samples. For pure PAN the S values decreased with increasing temperature, such behavior suggests that the conduction mechanism of pure PAN film could be correlated barrier hopping (CBH) [42]. On the other hand, for 10 wt.% SFO doped PAN nanocomposite sample the S values increased with increasing temperature. This means that the conduction mechanism of non-overlapping small polaron tunneling (NSPT) is predominant [43]. In the case of PAN doped with 10wt.% NCO NPs, the exponent S is almost around 0.8 and seems to be independent of temperature. Therefore, the conduction mechanism is of quantum mechanical tunneling (QMT) type [44].

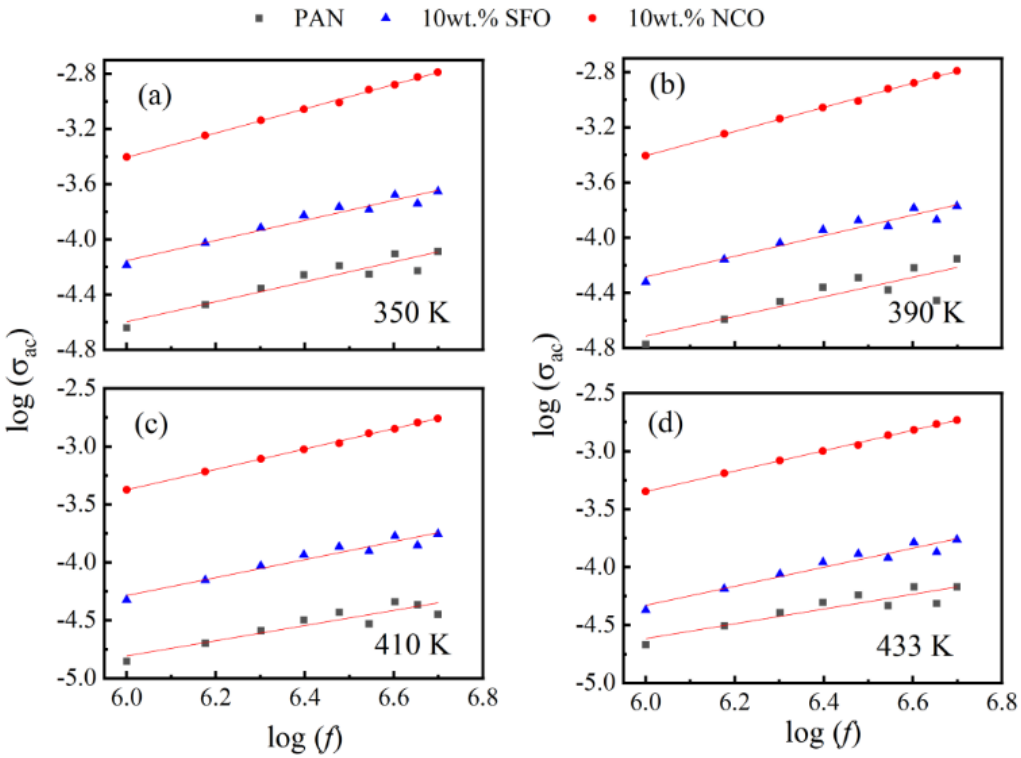

Fig 13: Frequency dependence of AC conductivity of the PAN, PAN doped 10wt.% SFO and NCP nanocomposite films at different temperatures. The solid lines are the fitting according to Eq. 6.

Table 2: Listed are the activation energy, the ac conductivity, *E*a, σ_{ac}, (Ω^{-1} m^{-1}), the frequency exponent, *S*, for pure PAN, PAN loaded with 10 wt.% SFO as well as NCO at different levels of temperatures.

Samples	Ea (eV)	σ_{ac} x 10^{-4} (Ω^{-1} m^{-1})					Frequency exponent, S, values			
		338K	348K	358K	378K	428K	350K	390K	410 K	433 K
PAN	0.28	1.03	1.63	1.44	1.68	1.9	0.723	0.710	0.654	0.637
10 wt. %NCO	0.64	21.12	22.51	21.83	23.77	25.34	0.728	0.747	0.775	0.821
10 wt.% SFO	0.27	2.68	4.13	4.1	4.05	5.49	0.879	0.876	0.879	0.882

4. Conclusions

This article reports the comparative analyses of morphological, structural, dielectric, and optical properties of the 10 wt.% SFO and NCO NPs dispersed PAN matrix. In FTIR spectra, increasing the peak intensities upon the desperation of SFO NPs in the PAN matrix compared with NCO NPs indicated a strong interaction of SFO NPs with the PAN functional groups. Both XRD and FE-SEM showed that the added nanofillers are dispersed inside the polymer matrix and influenced the degree of crystallinity and surface morphology of PAN. The incorporation of SFO NPs leads to an increment of PAN crystallinity. On the other hand, NCO addition reduced the crystallinity. DSC data showed that both SFO and NCO nanoparticles reduce (Tc) compared to pure PAN while the TGA results demonstrate that the PAN loaded with 10 wt.% NCO nanocomposites are more thermally stable compared to other samples. Compared to the pure PAN and SFO-doped PAN nanocomposite sample, the PAN doped with 10 wt.% NCO not only showed higher dielectric permittivity but also had lower dielectric loss. The comparison also showed that NCO NPs improved the ac conductivity of PAN more effectively than SFO NPs.

Finally, the outcome results of this work revealed that the physical properties of PAN are nanofiller dependent and could be controlled by incorporating a suitable amount of both SFO and NCO nanoparticles into the polymer matrix. The 10 wt.% NCO NPs/PAN showed superior properties such as higher dielectric permittivity, ac conductivity, and lower dielectric losses compared to those of the same SFO nanocomposite film implying that these nanocomposites could be a potential candidate for energy storage and capacitor applications.

Acknowledgment

The authors would like to thank Botany Dept, Faculty of science and Fayoum University for supporting the publication of this work.

Author Contributions

All authors have contributed to publishing this work. W. Shoubak prepared the samples and performed the dielectric measurement. A. Hassan supported the performance of the sample characterization. S. Mahrous explained the dielectric behavior of the studied samples while A. Hassen suggested the point of research and analyzed all obtained data. All authors contributed to writing the article. The corresponding author reviewed the manuscript and finalized it for publication.

Declaration of Competing Interest

The authors declare that they have no known competing financial interests or personal relationships that could have appeared to influence the work reported in this paper.

References

[1] Güneri, E., Kariper, A. (2012). Optical properties of amorphous CuS thin films deposited chemically at different pH values. Journal of Alloys and Compounds, 516, 20-26..

[2] Zihlif, A. M., Faduos, A. S., Ragosta, G. (2013). Optoelectrical properties of polymer composite: polystyrene-containing iron particles. Journal of Thermoplastic Composite Materials, 26(9), 1180-1191..

[3] Stepanov A.L. ''Optical Properties of Polymer Nanocomposites with Functionalized Nanoparticles (2018) '' Elsevier Inc, https://doi.org/10.1016/b978-0-12-814064-2. 00010-x.

[4] Jin, X., Ni, Q. Q., Fu, Y., Zhang, L., Natsuki, T. (2012). Electrospun nanocomposite polyacrylonitrile fibers containing carbon nanotubes and cobalt ferrite. Polymer composites, 33(3), 317-323.

[5] Palade, S., Pantazi, A., Vulpe, S., Berbecaru, C., Ţucureanu, V., Oprea, O., Dragoman, D. (2017). Tunable dielectric properties in polyacrylonitrile/multiwall carbon nanotube composites. Polymer Composites, 38(8), 1741-1748.

[6] DEMIRSOY, N., Nuray, U. C. A. R., Aysen, O. N. E. N., KIZILDAG, N. (2015). Nanocomposite Nanofibers of Polyacrylonitrile (PAN) and Silver Nanoparticles (AgNPs) Electrospun from Dimethylsulfoxide. Marmara Fen Bilimleri Dergisi, 27, 16-18.

[7] Su, Y., Zhang, W., Lan, J., Sui, G., Zhang, H., Yang, X. (2020). Flexible reduced graphene oxide/polyacrylonitrile dielectric nanocomposite films for high-temperature electronics applications. ACS Applied Nano Materials, 3(7), 7005-7015.

[8] Xu, Q., Xu, L., Cao, W., Wu, S. (2005). A study on the orientation structure and mechanical properties of polyacrylonitrile precursors. Polymers for advanced technologies, 16(8), 642-645.

[9] Xu, Q., Xu, L., Cao, W., Wu, S. (2005). A study on the orientation structure and mechanical properties of polyacrylonitrile precursors. Polymers for advanced technologies, 16(8), 642-645.

[10] Aoki, Y., Watanabe, M. (1992). Morphological, thermal, and rheological properties of nylon/acrylonitrile-butadiene-styrene alloys. Polymer Engineering & Science, 32(13), 878-885.

[11] Wan, L. S., Xu, Z. K., Huang, X. J., Wang, Z. G., Ye, P. (2005). Hemocompatibility of poly (acrylonitrile-co-N-vinyl-2-pyrrolidone) s: swelling behavior and water states. Macromolecular bioscience, 5(3), 229-236.

[12] Wang, Z. G., Wan, L. S., Xu, Z. K. (2007). Surface engineerings of polyacrylonitrile-based asymmetric membranes towards biomedical applications: An overview. Journal of Membrane Science, 304(1-2), 8-23.

[13] Guo, Z., Kim, T. Y., Lei, K., Pereira, T., Sugar, J. G., Hahn, H. T. (2008). Strengthening and thermal stabilization of polyurethane nanocomposites with silicon carbide nanoparticles by a surface-initiated-polymerization approach. Composites Science and Technology, 68(1), 164-170.

[14] McHenry, M. E., Johnson, F., Okumura, H., Ohkubo, T., Ramanan, V. R. V., Laughlin, D. E. (2003). The kinetics of nanocrystallization and microstructural observations in FINEMET, NANOPERM and HITPERM nanocomposite magnetic materials. Scripta Materialia, 48(7), 881-887.

[15] Stankovich, S., Dikin, D. A., Dommett, G. H., Kohlhaas, K. M., Zimney, E. J., Stach, E. A., Ruoff, R. S. (2006). Graphene-based composite materials. nature, 442(7100), 282-286.

[16] Wang, H. Z., Yao, B., Xu, Y., He, Q., Wen, G. H., Long, S. W., Gao, L. L. (2012). Improvement of the coercivity of strontium hexaferrite induced by substitution of Al3+ ions for Fe3+ ions. Journal of alloys and compounds, 537, 43-49.

[17] Dhage, V. N., Mane, M. L., Keche, A. P., Birajdar, C. T., Jadhav, K. M. (2011). Structural and magnetic behaviour of aluminium doped barium hexaferrite nanoparticles synthesized by solution combustion technique. Physica B: Condensed Matter, 406(4), 789-793.

[18] Zi, Z. F., Sun, Y. P., Zhu, X. B., Yang, Z. R., Song, W. H. (2008). Structural and magnetic properties of SrFe12O19 hexaferrite synthesized by a modified chemical co-precipitation method. Journal of Magnetism and Magnetic Materials, 320(21), 2746-2751.

[19] Shoubak, W. M., Hassan, A., Mahrous, S., Hassen, A. (2024). Controlling the physical properties of polyacrylonitrile by strontium hexaferrite nanoparticles. Polymer Bulletin,81, 697-718.

[20] Wei, T. Y., Chen, C. H., Chien, H. C., Lu, S. Y., Hu, C. C. (2010). A cost-effective supercapacitor material of ultrahigh specific capacitances: spinel nickel cobaltite aerogels from an epoxide-driven sol–gel process. Advanced materials, 22(3), 347-351.

[21] Feng, L., Zhu, Y., Ding, H., & Ni, C. (2014). Recent progress in nickel based materials for high performance pseudocapacitor electrodes. Journal of Power Sources, 267, 430-444.

[22] Dhibar, S., Malik, S. (2020). Morphological modulation of conducting polymer nanocomposites with nickel cobaltite/reduced graphene oxide and their subtle effects on the capacitive behaviors. ACS Applied Materials & Interfaces, 12(48), 54053-54067.

[23] Liu, S., An, C., Chang, X., Guo, H., Zang, L., Wang, Y., Jiao, L. (2018). Optimized core–shell polypyrrole-coated NiCo 2 O 4 nanowires as binder-free electrode for high-energy and durable aqueous asymmetric supercapacitor. Journal of Materials Science, 53, 2658-2668.

[24] Albohani, S., Sundaram, M., Laird, D. (2017). Polymer templated nickel cobaltate for energy storage. Renewable energy and environmental sustainability, 2, 9.
[25] Rashti, A., Wang, B., Hassani, E., Feyzbar-Khalkhali-Nejad, F., Zhang, X., Oh, T. S. (2020). Electrophoretic deposition of nickel cobaltite/polyaniline/rGO composite electrode for high-performance all-solid-state asymmetric supercapacitors. Energy & Fuels, 34(5), 6448-6461.
[26] Sami, S. K., Siddiqui, S., Feroze, M. T., Chung, C. H. (2017). Electrodeposited nickel–cobalt sulfide nanosheet on polyacrylonitrile nanofibers: a binder-free electrode for flexible supercapacitors. Materials Research Express, 4(11), 116309.
[27] Shoubak, W. M., Hassan, A., Mahrous, S., Hassen, A. (2023). Improving the electrochemical and physical properties of nickel cobaltite/polyacrylonitrile nanocomposites for supercapacitor applications. Physica Scripta, 98(10), 105927.
[28] Rehan, M., Nada, A. A., Khattab, T. A., Abdelwahed, N. A., Abou El-Kheir, A. A. (2020). Development of multifunctional polyacrylonitrile/silver nanocomposite films: Antimicrobial activity, catalytic activity, electrical conductivity, UV protection and SERS-active sensor. Journal of Materials Research and Technology, 9(4), 9380-9394
[29] Mosleh, Z., Kameli, P., Poorbaferani, A., Ranjbar, M., Salamati, H. (2016). Structural, magnetic and microwave absorption properties of Ce-doped barium hexaferrite. Journal of Magnetism and Magnetic Materials, 397, 101-107
[30] Basak, M., Rahman, M. L., Ahmed, M. F., Biswas, B., Sharmin, N. (2022). The use of X-ray diffraction peak profile analysis to determine the structural parameters of cobalt ferrite nanoparticles using Debye-Scherrer, Williamson-Hall, Halder-Wagner and Size-strain plot: Different precipitating agent approach. Journal of Alloys and Compounds, 895, 162694.
[31] Tarani, E., Arvanitidis, I., Christofilos, D., Bikiaris, D. N., Chrissafis, K., Vourlias, G. (2023). Calculation of the degree of crystallinity of HDPE/GNPs nanocomposites by using various experimental techniques: a comparative study. Journal of Materials Science, 58(4), 1621-1639.
[32] Zhang, H., Quan, L., Gao, A., Tong, Y., Shi, F., Xu, L. (2020). Thermal analysis and crystal structure of poly (acrylonitrile-co-itaconic acid) copolymers synthesized in water. Polymers, 12(1), 221.
[33] Gupta A. K., Chand N., Singh R., Mansingh A. (1979). Dielectric study of polyacrylonitrile, poly-2-hydroxyethyl methacrylate and their copolymers. European Polymer Journal, 15(2): 129-136
[34] Iqbal, M. J., Ashiq, M. N., Gul, I. H. (2010). Physical, electrical and dielectric properties of Ca-substituted strontium hexaferrite (SrFe12O19) nanoparticles synthesized by co-precipitation method. Journal of Magnetism and Magnetic Materials, 322(13), 1720-1726
[35] Damm, C., Münstedt, H., Rösch, A. (2008). The antimicrobial efficacy of polyamide 6/silver-nano-and microcomposites. Materials Chemistry and Physics, 108(1), 61-66.
[36] Mahrous S., Hanfy T. A. (2009). Dielectric analysis of chlorinated polyvinyl chloride stabilized with di-n-octyltin maleate. Journal of applied polymer science, 113(1): 316-320.
[37] Aziz, S. B., Abidin, Z. H. Z., Arof, A. K. (2010). Influence of silver ion reduction on electrical modulus parameters of solid polymer electrolyte based on chitosan-silver triflate electrolyte membrane. Express Polym. Lett, 4, 300-310.
[38] El-Sayed, S., Sayed, A. M. E. (2021). Influence of the sol–gel-derived nano-sized TiO2 and Y2O3 in improving the optical and electric properties of P (VAc/MMA). Brazilian Journal of Physics, 51(6), 1584-1596.
[39] Hanafy T. A., Elbanna K., El-Sayed S., Hassen A. (2011). Dielectric relaxation analysis of biopolymer poly (3-hydroxybutyrate). Journal of Applied Polymer Science, 121(6): 3306-3313
[40] Garg, A., Parmar, L. K., Garg, T., Dager, H. S., Bhardwaj, P., Yadav, A. (2024). Structural analysis and dielectric behavior of low-temperature synthesized nickel cobaltite. Chemical Physics Impact, 100457.
[41] Jonscher, A. K. (1999). Dielectric relaxation in solids. Journal of Physics D: Applied Physics, 32(14), R57.
[42] Hassen, A., Hanafy, T., El-Sayed, S., Himanshu, A. (2011). Dielectric relaxation and alternating current conductivity of polyvinylidene fluoride doped with lanthanum chloride. Journal of Applied Physics, 110(11).
[43] Ghosh, A. (1990). Transport properties of vanadium germanate glassy semiconductors. Physical Review B, 42(9), 5665.
[44] Jayakumar, T., Raja, C. R., Arumugam, S. (2020). Structural, Magnetic and Optical Analysis of Pb 2+- and Ce 3+ -Doped Strontium Hexaferrite. Journal of Superconductivity and Novel Magnetism, 33, 2451-2458.